



Contents lists available at ScienceDirect

Journal of the Mechanical Behavior of Biomedical Materials

journal homepage: www.elsevier.com/locate/jmbbm

Improving tissue expansion protocols through computational modeling

Taeksang Lee^a, Elbert E. Vaca^b, Joanna K. Ledwon^b, Hanah Bae^b, Jolanta M. Topczewska^b, Sergey Y. Turin^b, Ellen Kuhl^c, Arun K. Gosain^b, Adrian Buganza Tepole^{a,*}

^a School of Mechanical Engineering, Purdue University, West Lafayette, IN 47907, USA

^b Ann and Robert H. Lurie Children's Hospital of Chicago, Feinberg School of Medicine, Northwestern University, Chicago, IL 60611, USA

^c Departments of Mechanical Engineering, Bioengineering, and Cardiothoracic Surgery, Stanford University, CA 94305, USA

ARTICLE INFO

Keywords:

Tissue expansion
Skin
Remodeling
Growth
Isogeometric analysis

ABSTRACT

Tissue expansion is a common technique in reconstructive surgery used to grow skin *in vivo* for correction of large defects. Despite its popularity, there is a lack of quantitative understanding of how stretch leads to growth of new skin. This has resulted in several arbitrary expansion protocols that rely on the surgeon's personal training and experience rather than on accurate predictive models. For example, choosing between slow or rapid expansion, or small or large inflation volumes remains controversial. Here we explore four tissue expansion protocols by systematically varying the inflation volume and the protocol duration in a porcine model. The quantitative analysis combines three-dimensional photography, isogeometric kinematics, and finite growth theory. Strikingly, all four protocols generate similar peak stretches, but different growth patterns: Smaller filling volumes of 30 ml per inflation did not result in notable expander-induced growth neither for the short nor for the long protocol; larger filling volumes of 60 ml per inflation trigger skin adaptation, with larger expander-induced growth in regions of larger stretch, and more expander-induced growth for the 14-day compared to the 10-day expansion protocol. Our results suggest that expander-induced growth is not triggered by the local stretch alone. While stretch is clearly a driver for growth, the local stretch at a given point is not enough to predict the expander-induced growth at that location. From a clinical perspective, our study suggests that longer expansion protocols are needed to ensure sufficient growth of sizable skin patches.

1. Introduction

Tissue expansion is a popular technique in reconstructive surgery to grow skin *in vivo* in order to correct large cutaneous defects (Marcus and Horan, 1990). This technique was introduced in 1957 by Neumann (1957) and has since become ubiquitous to reconstruct breasts after mastectomy, to resurface giant nevi, and to treat burn wounds (Bakhshaeekia, 2013; Radovan, 1982; Rivera et al., 2005). Tissue expansion relies on the unique capacity of living tissue to adapt to mechanical loading through growth and remodeling (De Filippo and Atala, 2002; Taber, 1995). Yet, despite the popularity of this procedure, we lack a quantitative understanding of how exactly deformation leads to the growth of new tissue. Not surprisingly, numerous arbitrary protocols have been proposed, depending on the surgeon's experience, training, and personal preference.

In tissue expansion, the surgeon subcutaneously inserts a medical device resembling a balloon called the tissue expander. The device is filled with saline solution at different time points over the course of several weeks. At the end of the inflation process, the expanders are

removed and the skin stays as a dome-like structure revealing growth or, equivalently, permanent area changes. In the clinical setting, the surgeon has two main variables to control the tissue expansion process: inflation timing and inflation volume. The optimal design of a skin expansion protocol remains controversial, while some physicians advocate for rapid expansion others favor a longer protocol; some propose to inflate the expander to a larger volume while others prefer smaller amounts of fluid at each inflation step (Gosain et al., 2009; Iwahira and Maruyama, 1993; Khalatbari and Bakhshaeekia, 2013; Pamplona et al., 2014). Here we explore four different protocols of expansion in a porcine model to compare the effect of short or long protocol times, and small or large inflation volumes on skin growth and remodeling.

Another important question when new skin is created in response to stretch is whether or not there are changes in the tissue microstructure that accompany the growth process. While it is apparent that the new tissue looks and feels very similar to the original skin, some remodeling trends have been reported at the microscopic scale (Beauchene et al., 1989; Musteo et al. 1989). The epidermis, the top layer of skin that is mainly composed of keratinocytes, generally becomes thicker following

* Corresponding author.

E-mail address: abuganza@purdue.edu (A.B. Tepole).

tissue expansion (VanderKolk et al., 1988). In the dermis, the bottom layer of skin that is primarily made up of collagen, the fiber morphology becomes more disorganized (Timmenga et al., 1990). Here we explore the effect of the four different expansion protocols on the skin microstructure by analyzing histological images.

Characterizing the mechanics of tissue expansion has the advantage that skin is a thin membrane exposed to the outside environment. Thus, imaging systems can be developed to study skin mechanics non-invasively *in vivo* over long periods of time. Here we use three-dimensional photography to capture the geometry of skin in the operating room. Three-dimensional photography based on stereo vision has made significant progress in the last decade. It is now possible to use handheld cameras to capture three-dimensional surfaces with a minimal experimental setup and high accuracy (Camison et al., 2017). The advantage of such system is that noninvasive measurements can easily be performed in clinical settings such as the operating room, either for an animal model as we show here, or for translation of this protocol to human patients, which we intend to do in the near future. The work presented here closely follows our previous work on skin expansion biomechanics (Buganza Tepole et al., 2015a, 2016, 2017). In our previous studies, we used multi-view stereo to capture three-dimensional geometries. Here we use three-dimensional photography instead of multi-view stereo, but continue to use the same methodology for the mechanical analysis as before. Our approach combines isogeometric kinematics and the continuum theory of finite growth. In addition to our previous methodology, here we collect punch biopsies at the end of the protocol for further histological analysis. The topology of the collagen network and the geometry of the epidermis are crucial for skin mechanical and frictional behavior (Limbert, 2014, 2017; Leyva-Mendivil et al., 2015, 2017). This auxiliary analysis allows us to study, for the first time, how growth of skin at the tissue scale is related to microstructure changes.

Isogeometric analysis relies on B-spline parameterizations of the geometry (Hughes et al., 2005). Isogeometric analysis is extremely well-suited for studying skin mechanics since B-spline basis functions can be constructed with high continuity, enabling thin shell descriptions (Buganza Tepole et al., 2015b) and a smooth representation of the geometry with a relatively coarse mesh (Buganza Tepole et al., 2016). Furthermore, we express all surfaces in terms of the same parameter domain, such that computation of the deformation gradient between any two configurations is easily achieved with curvilinear coordinates (Buganza Tepole et al., 2015a). To estimate the amount of total growth, we assume that the total deformation is a combination of prestrain, elastic deformation, and total growth, through a multiplicative split of the deformation gradient (Rodriguez et al., 1994). The underlying finite growth theory has become a well-established framework to describe the mechanical adaptation of biological tissues (Kuhl, 2014; Zoellner et al., 2013).

The work presented here sheds new light on the impact of inflation volume and protocol duration on the resulting skin deformation and growth patterns and further establishes new technologies that allow us to quantify skin growth and remodeling in an *in vivo* animal model over long periods of time.

2. Methods

2.1. Porcine model of skin expansion

Four different models of expansion are illustrated in Fig. 1. The protocols mimic different clinical expansion strategies. The effect of small versus large inflation volumes is studied by injecting either 30 ml or 60 ml at each inflation step. For the long expansion protocol, the total duration of the experiment is 14 days, with two inflation steps 7 days apart, for the shorter expansion protocol, the second inflation step is only 4 days prior to the end of the experiment resulting in a 10-day protocol.

The experimental methodology used in this study closely follows our prior work with the exception of using three-dimensional photography instead of multi-view stereo, and the additional collection of punch biopsies for histology at the end of the process (Buganza Tepole et al., 2015a, 2016, 2017). Briefly, animals are provided with food and water *ad libitum* per veterinary recommendations throughout the study. All animals undergo grid tattooing procedure at age 6–7 weeks, with tissue expander placement surgery performed 1 week after the tattooing procedure. Four square grids are tattooed on the back of an animal. For either the front or the back grids, one side is used for expansion while the contralateral side serves as control. To study the four different protocols, we used two animals, one for the small and one for the large volume protocols.

On the expander side, a two-stage rectangular tissue expander with 120 ml filling capacity (PMT Corporation, catalogue number #3610-06-02, Chanhassen, MN) is inserted subcutaneously underneath the grid and the incisions are sutured and left to heal. The tissue expanders are placed in the plane immediately superficial to the overlying muscle fascia, *i.e.* between muscle fascia and subcutaneous fat. This is the same plane in which tissue expanders are inserted clinically in humans. Once the animal has fully recovered from the expander placement surgery, the inflation protocol begins. At each inflation step, we use a syringe to inject the desired amount of saline solution into the expander through a remote inflation port.

To capture the geometry, we take three-dimensional photos immediately before and after each inflation step. We use a handheld commercial system (Vectra H1, Canfield, New Jersey). At the end of the tissue expansion protocol, the animals are sacrificed. Three-dimensional photos of the grids are taken on that day, first *in vivo* and then *ex vivo*, after the entire patch has been excised. Following three-dimensional photo acquisition *ex vivo*, punch biopsies are collected. For the control side a single biopsy is needed, while for the expanded size we harvest three samples, one at the apex of the expander, one at the periphery of the expander, and one at an intermediate location between the apex and the periphery as illustrated in Fig. 1. Model 1 is the 10-day expansion protocol with small inflation volumes, model 2 is 10-day expansion with large volumes, model 3 is the long, 14-day expansion with small volumes, and model 4 is the short expansion with large volumes.

2.2. Isogeometric analysis and finite growth theory

Isogeometric analysis relies on B-spline surface reconstruction (Chen et al., 2014). We start with the same tattooed grid for all the skin patches and assign the same initial parameter space, *i.e.*, same mesh, to every patch at all time points. B-splines can easily reconstruct smooth surfaces due to the availability of high order basis functions, even with a coarse set of control points (Buganza Tepole et al., 2015b). In our case, the grids provide a set of 121 material points that are fitted with quadratic B-splines using open source spline libraries (SINTEF, Norway). The parameter space is chosen to be $(\xi, \eta) \in [0, 10] \times [0, 10]$. Hence, for a given grid at a specific point in time, the surface $\mathcal{S}(\xi, \eta)$ is a mapping from the parameter space to the physical \mathbb{R}^3 space. Given a pair of surfaces, we compute the deformation gradient using the corresponding metric tensors associated with the surface embeddings. For example, given \mathcal{S}^o as reference and \mathcal{S}^f as the deformed surface, respectively, we construct the covariant base vectors

$$\mathbf{G}_1^o = \frac{\partial \mathcal{S}^o}{\partial \xi} \quad \text{and} \quad \mathbf{G}_2^o = \frac{\partial \mathcal{S}^o}{\partial \eta}, \quad (1)$$

for the reference surface, and

$$\mathbf{G}_1^f = \frac{\partial \mathcal{S}^f}{\partial \xi} \quad \text{and} \quad \mathbf{G}_2^f = \frac{\partial \mathcal{S}^f}{\partial \eta}, \quad (2)$$

for the deformed surface. Such base vectors span only the surface

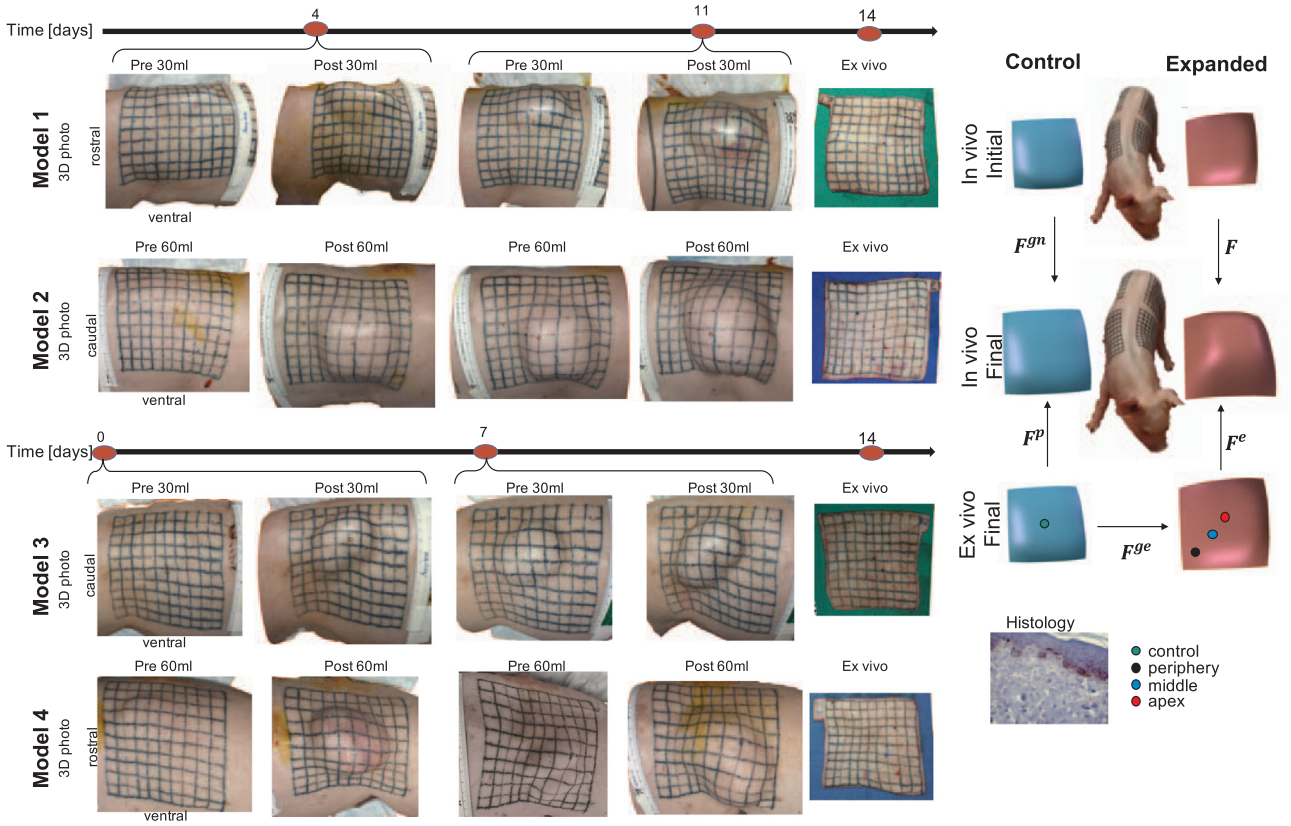


Fig. 1. The four different experimental protocols. Model 1 is 10-day expansion with small inflation volumes, model 2 is 10-day expansion with large volumes, model 3 is 14-day expansion with small volumes, and model 4 is 14-day protocol with large volumes. A tattooed grid defines the area of interest and allows for deformation tracking. Three-dimensional photos are taken at every inflation step, before and after inflation. At the end of the protocol, animals are sacrificed and grids excised. The deformations are analyzed using isogeometric analysis within the finite growth framework in which the deformation is a composition of prestrain F^p , deformation induced by expansion F , elastic deformation after expansion F^e , and total growth F^g . Additionally, natural growth F^{gn} is measured in the control patches in order to isolate the expander-induced growth. Punch biopsies are collected for the control and expanded grids to quantify changes in microstructure by analyzing histological slides. (For interpretation of the references to color in this figure legend, the reader is referred to the web version of this article.)

tangent space and we complement them with the surface normals

$$G_3^o = \frac{G_1^o \times G_2^o}{\|G_1^o \times G_2^o\|} \quad \text{and} \quad G_3^f = \frac{G_1^f \times G_2^f}{\|G_1^f \times G_2^f\|}. \quad (3)$$

The contravariant base vectors are defined via the identity $G_i \cdot G^j = \delta_i^j$. The deformation gradient is

$$F = G_i^o \otimes G^{i^f}, \quad (4)$$

where the summation convention was used. To account for finite volumetric growth, we multiplicatively splits the deformation gradient into total growth and elastic contributions, F^g and F^e (Taber and Chabert, 2002). Here, the total deformation gradient of the skin surface captures both, the *in vivo* expansion process F and the amount of prestrain F^p (Rausch and Kuhl, 2013). The determinant of the deformation gradient obeys the same split. In our case, the determinant of the deformation gradient is equivalent to the area change θ ,

$$F \cdot F^p = F^e \cdot F^g \quad \text{and} \quad \theta \cdot \theta^p = \theta^e \cdot \theta^g. \quad (5)$$

The tensors F and F^e are obtained from the expanded patch whereas F^p is calculated from the control patch by mapping the *ex vivo* control surface to the *in vivo* control surface. We can then calculate the total growth tensor, $F^g = F^{e-1} \cdot F \cdot F^p$. The total growth tensor can further be decomposed into two contributions, naturally-induced growth F^{gn} and expansion-induced growth F^{ge} ,

$$F^g = F^{ge} \cdot F^{gn} \quad \text{and} \quad \theta^g = \theta^{ge} \cdot \theta^{gn}. \quad (6)$$

In addition to changes in area, we compute changes in length along the two directions of interest. For any of the skin patches at day 0, the

vector G_1 corresponds to the longitudinal axis of the animal, while the vector G_2 is aligned with the transverse direction. These vectors, however, are not necessarily of unit length. We then define the unit vectors

$$E_1 = \frac{G_1}{\|G_1\|} \quad \text{and} \quad E_2 = \frac{G_2}{\|G_2\|}. \quad (7)$$

The deformations due to the expansion process along the two directions of interest are the stretches

$$\lambda_1 = \sqrt{E_1 \cdot C \cdot E_1} \quad \text{and} \quad \lambda_2 = \sqrt{E_2 \cdot C \cdot E_2}, \quad (8)$$

where $C = F^T \cdot F$ is the right Cauchy-Green deformation tensor. We further assume that prestrain and total growth leave the two directions unchanged,

$$F^p = \lambda_1^p E_1 \otimes E^1 + \lambda_2^p E_2 \otimes E^2 \\ F^g = \lambda_1^g E_1 \otimes E^1 + \lambda_2^g E_2 \otimes E^2, \quad (9)$$

such that a multiplicative split analogous to equation (5) is possible for the longitudinal and transverse deformations.

2.3. Histology analysis

Following excision of the skin patches, we collect punch biopsies at different locations as indicated in Fig. 1. For the control patch, only one sample is collected whereas for the expanded grids, three points are marked with different colors before excision and biopsies are taken *ex vivo*: at the apex (red), at an intermediate point (blue), and at the periphery of the expanded area (black). We use pentachrome staining to visualize the different constituents of skin. In this study we are

interested in the thickness of the epidermis and the collagen network morphology. Histological slides are processed with the OrientationJ plugin in imageJ (Schindelin et al., 2012) to quantify collagen orientation in the dermis (Rezakhaniha et al., 2012). For a given histological slide, we compute a coherency image which contains local alignment information normalized between 0 and 1. Briefly, for a given image $I(x, y)$, we compute the gradients $I_x = \partial I / \partial x$ and $I_y = \partial I / \partial y$ (Rezakhaniha et al., 2012). From these vector fields, we compute the tensor field \mathbf{J} ,

$$\mathbf{J} = \begin{pmatrix} \langle I_x, I_x \rangle_w & \langle I_x, I_y \rangle_w \\ \langle I_y, I_x \rangle_w & \langle I_y, I_y \rangle_w \end{pmatrix}, \quad (10)$$

where $\langle f, g \rangle_w = \int_w f \cdot g \, dA$ denotes the inner product and $w(x, y)$ is a Gaussian weighting function such that the inner product $\langle f, g \rangle_w$ serves as a smoothing filter with a kernel w . Coherency is then defined as

$$C(x, y) = \frac{\lambda_{\max} - \lambda_{\min}}{\lambda_{\max} + \lambda_{\min}}, \quad (11)$$

with λ_{\max} and λ_{\min} the largest and smallest eigenvalues of \mathbf{J} . We report the average of the coherency image. OrientationJ also outputs a distribution of the orientations over the entire image. We fit a Gaussian to the fiber distribution and define the standard deviation of such distribution as *dispersion*. Finally, we measure the thickness of the epidermis using imageJ with a novel tool proposed recently by our groups and described in detail in a separate publication (Turin et al., 2018).

3. Results

3.1. Total deformation

Fig. 1 shows the three-dimensional photographs obtained at each inflation step and Fig. 2 depicts the contour plots of the area change θ over the expanded three-dimensional geometries. As expected and in agreement with our previous studies (Buganza Tepole et al., 2011, 2016), strains are greater at the apex of the expander compared to the periphery. This can be appreciated also in Fig. 2, last column, which shows the deformation for specific points of the expanded patch. The red, blue, and black curves correspond to points at the apex, the middle, and the periphery respectively. The same expander was used in all models, however, when the expanders are not yet filled to their capacity, their shape can show some variation as seen in Fig. 1. Additionally, two of the expanders moved during the protocol. In model 1, the expander migrated anteriorly by approximately 2 cm. In model 4, the expander migrated posteriorly 1 cm, and ventrally 2 cm. Despite these displacements, the expanders all remained within the tattoo grid at sacrifice. Over the two weeks of the experiment, the overall trend is an increase in deformation at all points. Not all deformation is expander-induced strain. Some deformation is related to the natural growth of the animal measured on the control patches, see Tables 1, 2. Greater deformation is consistently seen for the apex point (red) in all expansion models. Surprisingly, the large volume protocols result in similar peak strain as the small volume protocols, see Table 2, first column. However, in the large volume models, the blue and black points show progressively less deformation, with $\theta \in [1.1, 2]$ at the end time point, whereas in the small volume protocols the deformation is similar for the three points of interest, $\theta \in [1.5, 2]$.

Fig. 3 shows the stretches $\lambda_1^F = \|\mathbf{F} \cdot \mathbf{E}_1\|_2$ and $\lambda_2^F = \|\mathbf{F} \cdot \mathbf{E}_2\|_2$ in the directions of interest. Recall that \mathbf{E}_1 is aligned with the longitudinal axis of the animal at the beginning of the protocol and \mathbf{E}_2 is a unit vector field in the transverse orientation. Similarly to what is seen in the total area plots, the stretches for the two principal directions show greater deformation in the apex and less in the periphery of the expanded area. Another trend that we have consistently observed in our previous studies is that stretches in the longitudinal axis are greater than transverse deformations (Buganza Tepole et al., 2015a).

3.2. Elastic deformation, prestrain, and growth

At the end of the expansion protocol, excision of the expanded patch reveals the elastic deformation \mathbf{F}^e while excision of the control patch allows quantification of the prestrain \mathbf{F}^p . Then, using \mathbf{F} from the previous section and employing equation (5) we calculate the total growth \mathbf{F}^g . We further use the control patch to measure the natural growth \mathbf{F}^{gn} . Fig. 4 shows the individual components of the area change for the different experimental models. The elastic area change θ^e follows the pattern of the total area change θ : Upon excision, the skin retracts the most in regions of highest *in vivo* area change. Prestrain fields θ^p are measured in the control patches, thus, they are not directly affected by the expansion procedure and have a less defined spatial pattern. There is some variation between the different animals. For model 1 and model 3, the prestrain is greater towards the ventral side of the animal whereas for models 2 and 4, the prestrain is overall lower and more uniform, see Table 1. The total growth for model 1 and model 3 is larger compared to models 2 and 4. For all protocols, the natural growth fields, measured on the control patches, have the lowest spatial variation among all the components of the deformation. This is also captured in the standard deviation values summarized in Table 1.

Growth attributed to the expansion process alone is the key component of deformation for this study. This deformation field, \mathbf{F}^{ge} , can be computed using equation (6) based on the total growth and natural growth fields. Since the natural growth fields have the lowest spatial variation, the heterogeneous patterns of the total growth fields are due to the expansion-induced growth. However, most of the total growth can be attributed to the natural growth of the animals. In other words, the total growth fields, measured in the expanded patches, have to be normalized by the natural growth seen in the control patches. The total growth field is always greater than 1, indicating that skin increases its area for all expansion protocols. However, as seen in the control patches, some growth would occur naturally even in the absence of an expander. The expander-induced growth field then captures the area changes with respect to the naturally grown skin, isolating the contribution of the expansion process. The contours corresponding to the expander-induced growth show that for the larger filling volumes, in model 2 and model 4, zones under larger deformation show larger growth, whereas for the small volume models there is no clear spatial pattern with relation to the expander placement, see Fig. 5.

For model 1 and model 3, which were inflated with 30 ml at each inflation step, the expander-induced growth at the points of maximum deformation (red curves in Fig. 2) is only 8% and 2%, respectively, see Table 3. In contrast, for model 2 and model 4, with 60 ml inflation steps, the apex point reaches a similar deformation as seen in model 1 and model 3, but in this case, expander-induced growth was as large as 22% and 27%. For the small volume protocols, models 1 and 3, for which the intermediate and periphery points show similar deformation history compared to the apical point, the expander-induced growth is also within a narrow range. For the large volume protocols, models 2 and 4, where the three points of interest show markedly different deformation history, the expander-induced growth also shows notable variation. As just reported, the apical point showed the greatest *in vivo* deformation and greatest expander-induced growth in models 2 and 4. The points between the apex and the periphery show intermediate values of deformation and also modest expander-induced growth. The periphery points were deformed the least in model 2 and model 4, and show negative expander-induced growth ($\theta^{ge} < 1$), i.e., the skin at these locations shrinks compared to the naturally grown skin. Calculating the components of the expansion-induced growth λ_1^{ge} and λ_2^{ge} in the two directions of interest reveals a similar trend compared to the area changes. The longitudinal axis of the animal, which experiences greater deformations, also presents higher growth values in that direction.

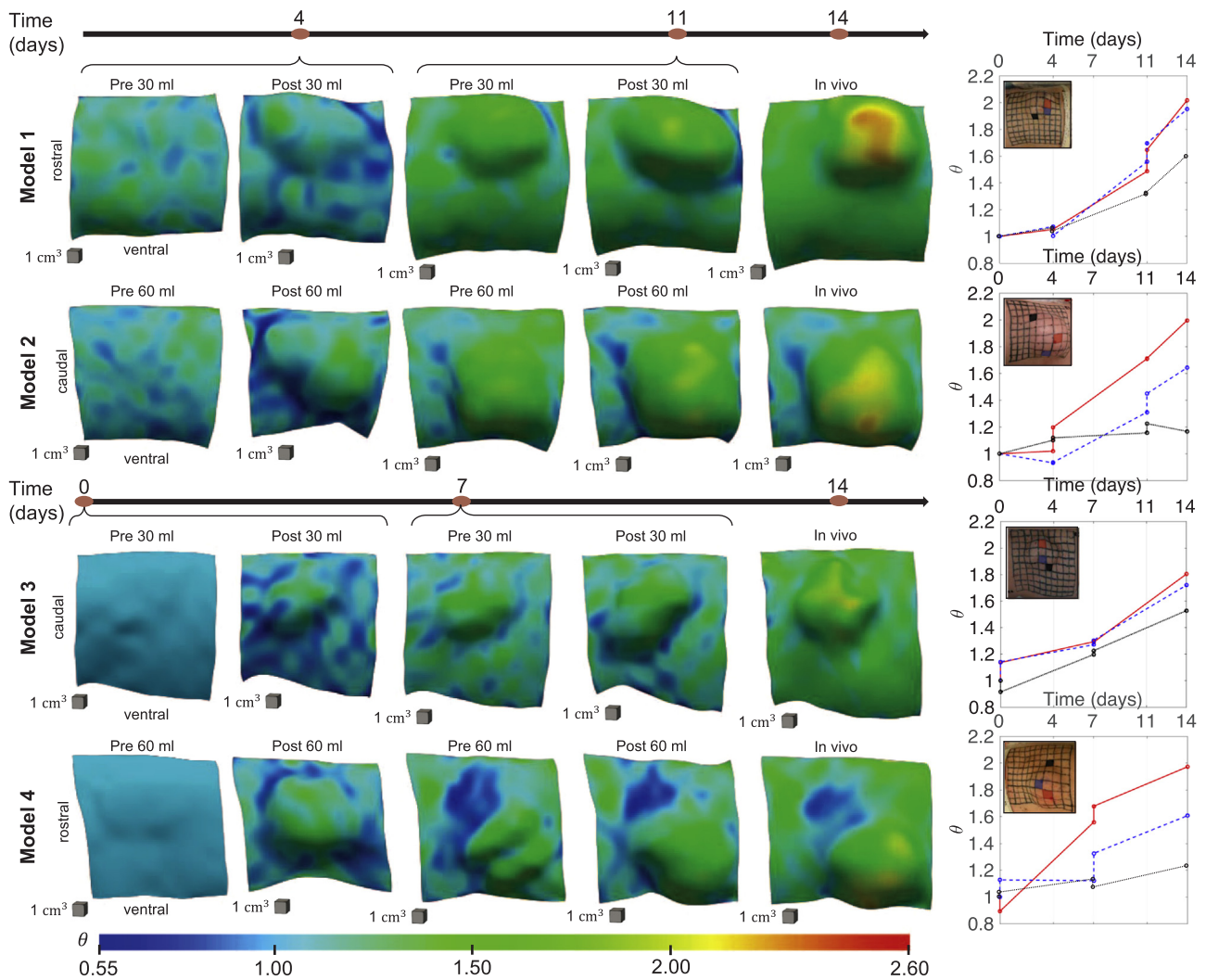


Fig. 2. Area change for the total deformation $\theta = \det(\mathbf{F})$ is calculated with respect to the initial *in vivo* state. The rows show the different inflation protocols: The last column shows the deformation for specific points of interest: The red curve corresponds to a point at the apex of the expander, the black curve is a point at the periphery, and the blue curve is an intermediate point. The overall trend is an increase in deformation, with the apex point (red) showing the greatest deformation followed by the intermediate (blue) and the periphery (black) points. Peak stretches are similar across all protocols. (For interpretation of the references to color in this figure legend, the reader is referred to the web version of this article.)

3.3. Changes in tissue microstructure

The incision for expander placement was made 2 cm away from the expander grid periphery; therefore, the area of expansion was remote from areas of the skin surgical scar. However, due to the natural foreign body response, a collagen capsule always forms around the tissue expander. This is observed clinically in humans as well. These capsules become firmer and thicker if there is a secondary insult such as radiation or infection. There was no infection in these animals and the peri-

prosthetic capsule was soft in all cases. Fig. 6 shows sample histological images representative of the expansion models. These images correspond to the apex point which was subjected to the greatest deformation and showed the highest expansion-induced growth. Table 4 summarizes the results from the histological analysis. The epidermal thickness increased in the expanded patches compared to the controls, which is evident from looking at the images with the naked eye and then confirmed with the measurements. Results from the OrientationJ plugin did not show clear differences between expanded skin and

Table 1

Average values and standard deviations for total deformation θ , elastic deformation θ^e , prestrain θ^p , total growth θ^g , and natural growth θ^{gn} calculated over the entire grid for each of the inflation models. Standard deviation over a skin patch is large for the components of the deformation directly affected by the expansion process. Natural growth, measured on the control patches, is a more homogeneous field for all models and hence shows lower standard deviation.

Model	Timing	Volume	θ		θ^e		θ^p		θ^g		θ^{gn}	
			avg	std	avg	std	avg	std	avg	std	avg	std
Model 1	Short	Small	1.47	0.23	1.20	0.19	1.22	0.17	1.49	0.20	1.38	0.10
Model 2	Short	Large	1.35	0.30	1.24	0.21	1.15	0.11	1.24	0.17	1.28	0.13
Model 3	Long	Small	1.36	0.18	1.18	0.22	1.30	0.17	1.39	0.19	1.37	0.11
Model 4	Long	Large	1.31	0.28	1.16	0.15	1.10	0.11	1.23	0.21	1.29	0.13

Table 2

Total deformation θ , elastic deformation θ^e , prestrain θ^p , total growth θ^g , and natural growth θ^{gn} are calculated for the three points of interest: Red (apex of the expander), Blue (intermediate point between the apex and the periphery), Black (periphery of the expander). The red point was consistently deformed the greatest in all models and the peak value was close for all cases (first column). Total growth in the small volume cases was lower at the apex compared to the large volume protocols regardless of whether the inflation was over 10 or 14 days. In contrast, total growth was higher in the blue and black points in the small volume models compared to the larger volumes.

Model	Points	θ	θ^e	θ^p	θ^g	θ^{gn}
Model 1	Red	2.02	1.64	1.17	1.45	1.34
	Blue	1.95	1.47	1.19	1.58	1.36
	Black	1.60	1.22	1.06	1.39	1.30
Model 2	Red	1.99	1.65	1.27	1.54	1.27
	Blue	1.64	1.58	1.19	1.23	1.23
	Black	1.17	1.16	1.17	1.19	1.39
Model 3	Red	1.80	1.60	1.18	1.32	1.30
	Blue	1.72	1.60	1.16	1.25	1.33
	Black	1.53	1.31	1.31	1.53	1.44
Model 4	Red	1.97	1.45	1.00	1.36	1.07
	Blue	1.61	1.26	1.05	1.34	1.21
	Black	1.23	1.06	1.04	1.22	1.47

controls. While in some cases the collagen network in the control case is thicker and more organized than the expanded patches, this is not true for all the models. In Fig. 6, the dermis is split into two sublayers. The papillary dermis is the top sublayer, just below the epidermis. The reticular dermis is the bottom sublayer. For the papillary dermis, coherency values are similar across all models and controls. The reticular coherency is slightly higher in the control cases, particularly in the 10-day expansion of model 1 and model 2. Interestingly, the papillary coherency is greater than the reticular coherency for both expanded skin and controls. The dispersion of the fiber orientation does not provide any clear difference between the expansion protocols and the controls. Nonetheless, it is clear that the papillary dermis is more organized, and thus has a lower dispersion of the fiber orientation, compared to the reticular dermis in both expanded skin and controls.

4. Discussion

Tissue expansion is a popular technique to grow skin *in situ*; yet, the parameters that drive this procedure remain poorly understood. This study was particularly motivated by the lack of consensus regarding the optimal volume and timing of inflations (Bakhshaeekia, 2013; Yang et al., 2011; Zeng et al., 2003). Quantitative tools to predict the effects of the different process parameters is an important step towards improving efficiency and making the technology more applicable. Equipped with an innovative experimental design, we are able to characterize the mechanics of small or large inflation volumes for short or long inflation protocols. Our method is based on three-dimensional photography, isogeometric kinematics, and finite growth theory.

Our results confirmed previous experimental and computational results with greater deformation at the apex of the expander compared to the periphery (Buganza Tepole et al., 2015a, 2016). Interestingly, the maximum deformation was similar in response to all four protocols regardless of the amount of fluid in each inflation step. There are several possible explanations for this non-intuitive observation. The total *in vivo* deformation is a combination of elastic deformation, natural growth, and expander-induced growth. Natural growth is measured in the control skin and not directly affected by the expansion process; however, it does vary from one animal to another. Therefore, comparing the total *in vivo* deformation between animals ignores this source of variation. In fact, in the small volume experiments, the animals showed greater natural growth, which could help explain why the peak values of deformation were similar across all protocols. It is also possible that the suprphysiological growth at the expanded sites could lead to systemic changes affecting natural growth on the rest of the animal, including skin in the control patches. Our previous work (Buganza Tepole et al., 2015a, 2016) together with this study confirms that natural growth of the animals is on the order of 1–2% per day. While our previous protocols consisted of different inflation volumes and time points of inflation, we previously reported that the deformation at day 15, at a volume of 150 ml, was 1.43, similar to the values reported here. Prestrain is also measured in the control patches and, thus, not directly affected by the expansion process. However, there is also some variability in prestrain between animals independently of the expansion protocols. In the experiments reported here, average values of prestrain for model 1 and model 3 are within the previously reported ranges from 1.24 to 1.44. Prestrains for model 2 and model 4, however,

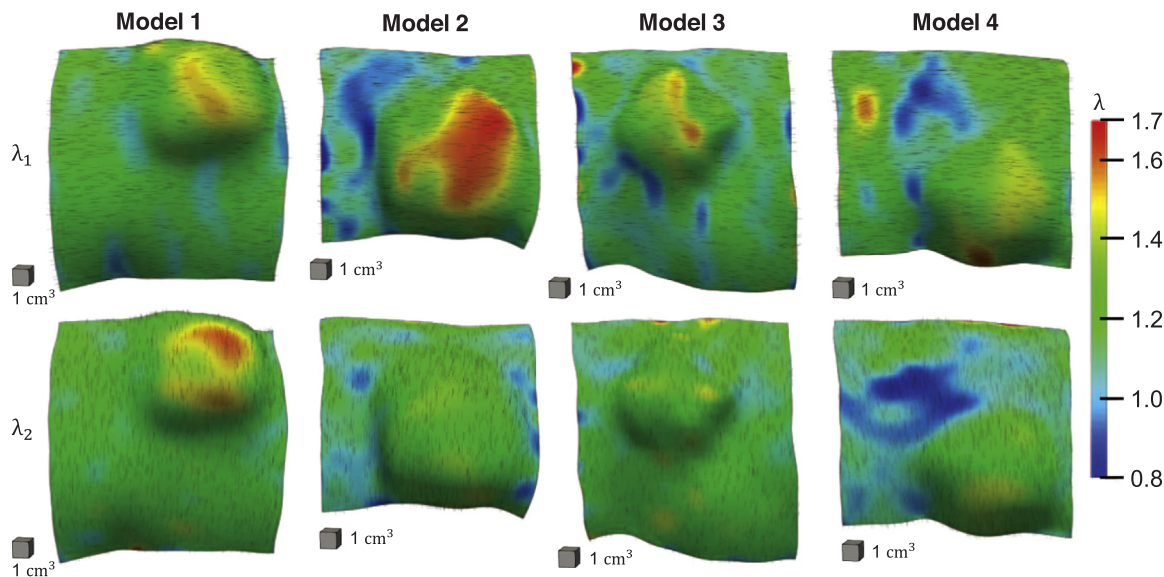


Fig. 3. Total deformation F calculated with respect to the initial *in vivo* state is used to compute the stretch along the two directions of interest: λ_1 is the stretch in the longitudinal axis of the animal E_1 , λ_2 is the stretch in the transverse direction E_2 . The columns show the contours of λ_1 and λ_2 for the different inflation protocols. The vector fields associated to the deformed configuration, $F \cdot E_1$ and $F \cdot E_2$, are also shown.

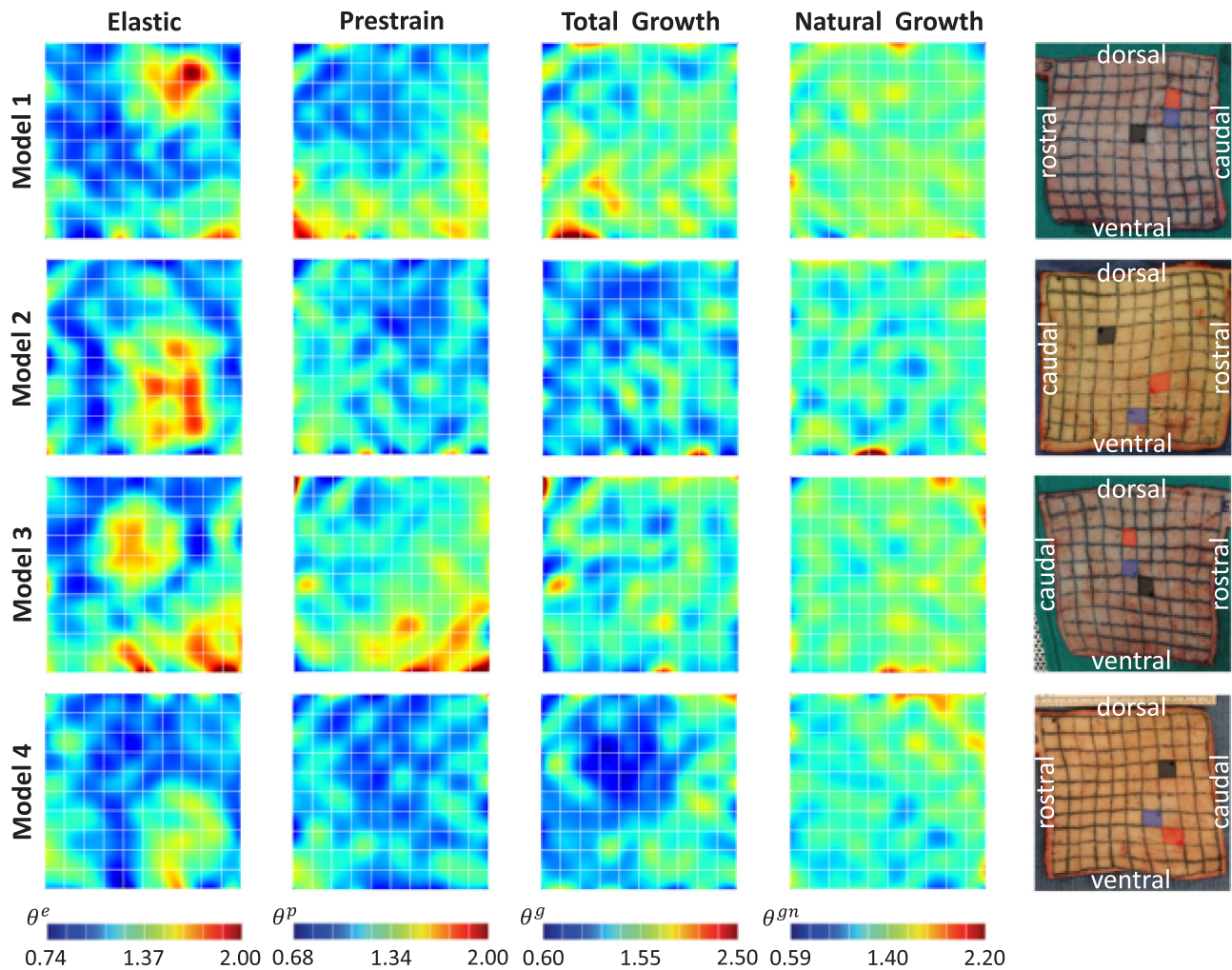


Fig. 4. Contour plots over the parameter space for elastic deformation θ^e , prestrain θ^p , total growth θ^g , and natural growth θ^{gn} . The elastic deformation reflects the pattern of the total deformation. Prestrain fields are calculated based on the control patch and not affected by the expansion process, nonetheless some spatial variation is observed as well as inter-specimen variability. Total growth is a combination of natural and expander induced growth. The natural growth fields are uniform in all cases.

are lower in this study, 1.10 and 1.15. Even in the presence of some variability, our data aligns with our previous observations.

For all four models, the average value of expander-induced growth was close to one, indicating little to no growth with respect to the natural growth field. This finding is not entirely surprising based on our previous work. We have reported expansion-induced growth of 1.54 for a 37-day expansion protocol (Buganza Tepole et al., 2015a) and 1.17 and 1.10 for two different 21-day protocols (Buganza Tepole et al., 2016). It is possible that 14 days is not long enough to capture significant amount of expander-induced growth over entire skin patches. However, our local contours reveal that some regions do indeed grow. Focusing on the apex, which was subjected to the largest deformation, we observe that for the small volume model 1 and model 3, the expander-induced growth was smaller compared to the large volume model 2 and model 4. This is important because for the apical points the elastic and total deformations were similar, suggesting that expander-induced growth may not just be a local effect. On the other hand, the intermediate and periphery points in the small volume experiments showed similar values of total deformation as the apex, and similar values of expander-induced growth. For the large volume experiments, the intermediate and periphery points showed progressively less deformation compared to the apex, and also less expander-induced growth. These findings support that the deformation pattern for a given patch is indeed related to the expander-induced growth field. One

possibility is that the difference in the expander-induced growth fields between the small and large volume experiments is only attributed to animal variability. However, in light of our previous work (Buganza Tepole et al., 2015a, 2016), and also current understanding of skin mechanobiology (Wong et al., 2011; Derderian et al., 2005; Silver et al., 2003), we hypothesize that the expander-induced growth field is a function of the spatial pattern of deformation but not just the deformation at a local point. In other words, knowing the total deformation at a single location is not enough to anticipate the growth at that location. The data presented here are only a macroscopic mechanics description and further experiments are needed at the cellular scale to clarify the biological pathways involved in the growth process. Nevertheless, this non-locality hypothesis is also supported by our previous studies that found an expander-induced growth field which was not perfectly aligned with the expansion-induced deformation, but rather seemed to be a smoothed version of this deformation field (Buganza Tepole et al., 2015a, 2016). The literature on skin mechanobiology also points towards the coupling of non-local signals, mainly, the production of growth factors that diffuse and trigger growth beyond points of maximum deformation (Jiang et al., 2012; Silver et al., 2003; Wang and Thampatty, 2006). These secondary mechanotransduction pathways include transforming growth factors β_1 and α (TGF- β_1 , TGF- α) (Fuchs and Raghavan, 2002; Wang et al., 2007). Growth factors inherently require consideration of diffusion and could help explain the

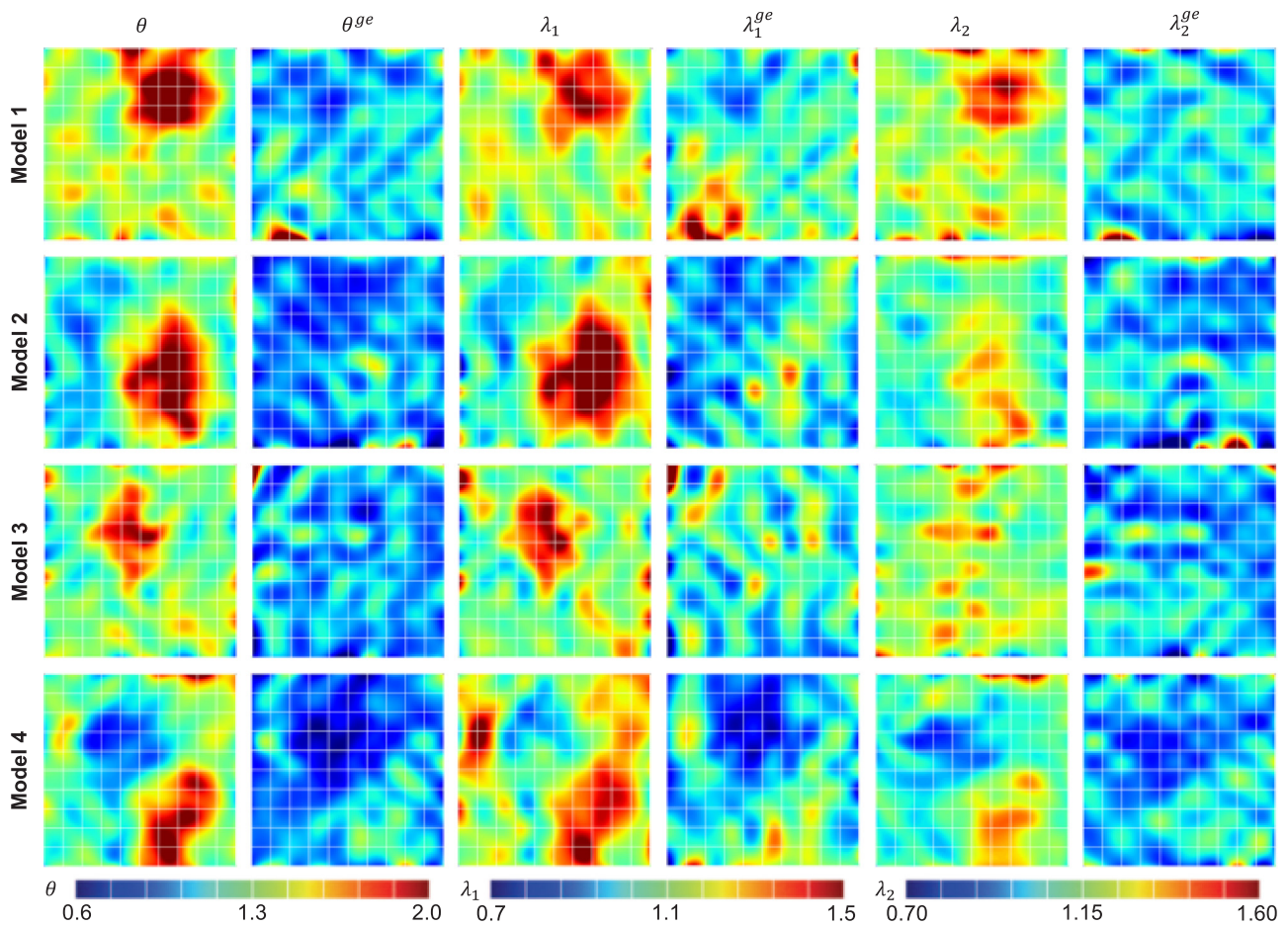


Fig. 5. Contour plots over the parameter space for total *in vivo* deformation $\theta = \det(\mathbf{F})$, and expander-induced area growth $\theta^{ge} = \det(\mathbf{F}^{ge})$, as well as the split in the two directions of interest, $\lambda_1 = \|\mathbf{F} \cdot \mathbf{E}_1\|_2$ and $\lambda_2 = \|\mathbf{F} \cdot \mathbf{E}_2\|_2$ for the total deformation, and $\lambda_1^{ge} = \|\mathbf{F}^{ge} \cdot \mathbf{E}_1\|_2$ and $\lambda_2^{ge} = \|\mathbf{F}^{ge} \cdot \mathbf{E}_2\|_2$ for the expander-induced growth. The large volume protocols (models 2 and 4) show greater expander-induced growth at the apex of the expander which corresponds to the regions of higher total deformation. The small volume models do not show a well-defined spatial trend. Calculating the components of this growth field on the two directions of interest shows that the longitudinal direction \mathbf{E}_1 grows more in response to stretch compared to the transverse orientation.

Table 3

Area growth attributed to the expansion process alone, θ^{ge} , and split in the two orientations of interest λ_1^{ge} and λ_2^{ge} . Values are calculated for the three points of interest: Red (apex of the expander), Blue (intermediate point between the apex and the periphery), Black (periphery of the expander). The red point, which was consistently deformed the greatest in all models, shows greater expansion-induced growth for the large volume models but not for the small volume ones. Expander-induced growth occurs primarily in the longitudinal axis of the animal.

Model	Points	θ^{ge}	λ_1^{ge}	λ_2^{ge}
Model 1	Red	1.08	0.99	1.07
	Blue	1.16	1.10	1.06
	Black	1.07	1.04	1.03
Model 2	Red	1.22	1.25	0.99
	Blue	1.00	1.08	0.94
	Black	0.85	0.90	0.95
Model 3	Red	1.02	1.12	0.91
	Blue	0.94	1.00	0.93
	Black	1.06	1.02	1.06
Model 4	Red	1.27	1.19	1.08
	Blue	1.11	1.06	1.06
	Black	0.83	0.90	0.92

mismatch between total deformation and expander-induced growth. We also remark that the expanders in models 1 and 4 moved approximately 2 cm from their initial location in the grid. This could add an extra variation to the final expander-induced growth pattern. Nonetheless, despite this movement, the expander-induced growth field in model 4, one of the large volume protocols, did resemble the total deformation field, similar to the other large volume case, model 2. Both small volume models show expander-induced growth patterns that do not resemble the total deformation, even though only the expander in model 1 moved.

A closer look at the microstructure reveals a change in epidermal thickness in the expanded patches consistent with previous reports (Alex et al., 2001; Austad et al., 1982; Johnson et al., 1988). Epidermal thickness at the apex increased in all expansion protocols. Interestingly, thickness increased more on the small volume model 1 and model 3 compared to the large volume models 2 and 4. This is the opposite trend with respect to expander-induced growth at this location. We remark that expansion-induced growth corresponds to area changes normalized by the amount of naturally grown skin. Therefore, total growth may offer a better understanding of epidermal thickening. Total growth at the apex was similar between small and large volume protocols. This is because the natural growth in the small volume modes was larger compared to the large volume cases. Nevertheless, total growth at the apex was still higher in the large volume protocols. Further work is needed to clarify this result. Our next step is to directly quantify proliferation rates of keratinocytes rather than thickness values alone.

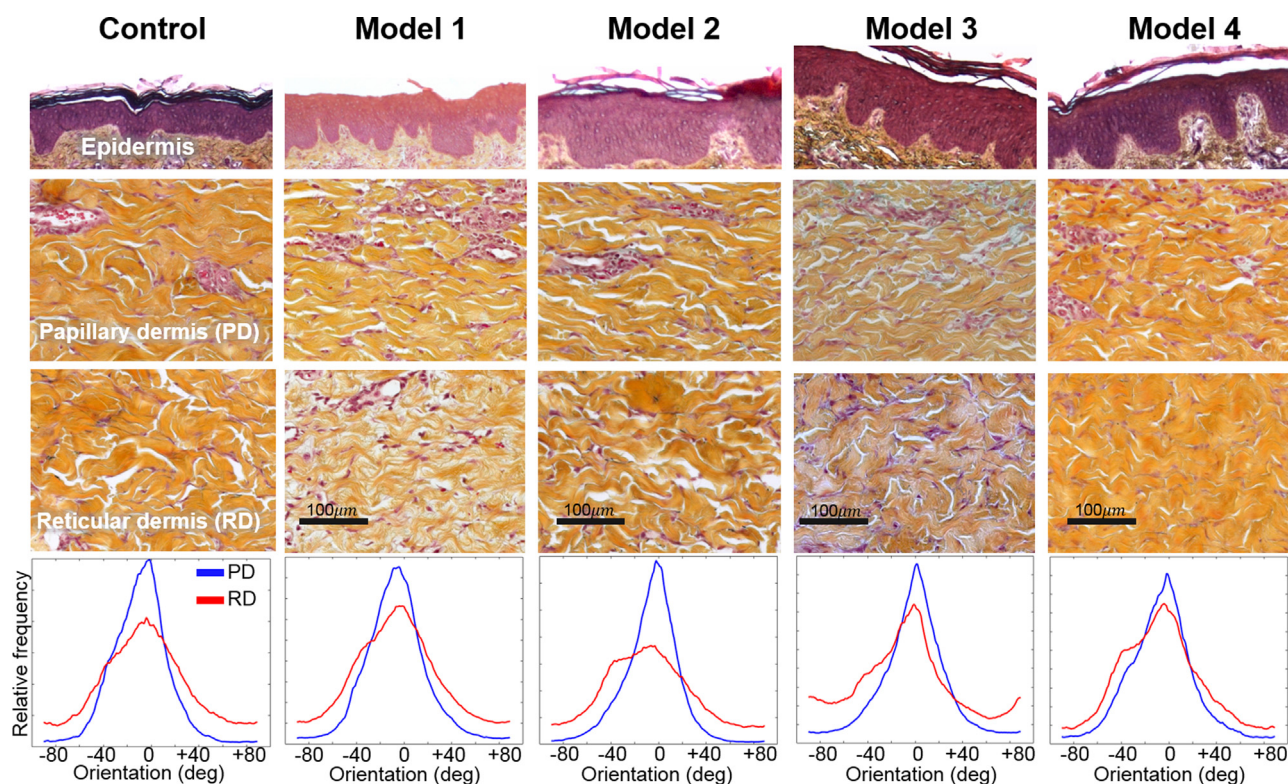


Fig. 6. Pentachrome-stained histological slides corresponding to the apex point of the different models as well as a representative control. Collagen is visible in orange while cells are stained in purple. As expected, the epidermis, the top layer of the skin primarily made out of keratinocyte cells, thickens upon expansion (see also Table 4). The dermis is divided into two sublayers, the papillary dermis is immediately below the epidermis and the reticular dermis is underneath the papillary layer. Collagen bundles in the control skin appear thicker compared to the expansion protocols but no trend could be identified (see Table 4). (For interpretation of the references to color in this figure legend, the reader is referred to the web version of this article.)

Table 4

Analysis of histological slides. Thickness of the epidermis was determined with imageJ with a method proposed by our group (Turin et al., 2018). Collagen orientation was done with the ImageJ plugin OrientationJ (Rezakhaniha et al., 2012) which outputs coherency and dispersion of the orientation distribution. Coherency is a local metric of alignment normalized between 0 and 1 whereas dispersion relates to the spread of the fiber orientation distribution of an entire image. No clear trend is seen between expanded and control patches regarding the orientation distribution. However, thickness of the epidermis was higher in expanded patches compared to controls.

Model	Epidermis thickness [μm]	Papillary coherency [-]	Reticular coherency [-]	Papillary dispersion [deg]	Reticular dispersion [deg]
Model 1	96.8 (sd 8.9)	0.46 (sd 0.01)	0.41 (sd 0.01)	15.11 (sd 1.08)	25.43 (sd 3.01)
Model 2	60.7 (sd 5.3)	0.57 (sd 0.02)	0.49 (sd 0.02)	13.02 (sd 1.20)	27.06 (sd 1.09)
Model 3	76.7 (sd 6.9)	0.48 (sd 0.02)	0.44 (sd 0.03)	15.25 (sd 1.42)	23.39 (sd 4.00)
Model 4	64.5 (sd 3.5)	0.50 (sd 0.02)	0.43 (sd 0.02)	16.96 (sd 3.82)	23.99 (sd 3.82)
Control 1	58.4 (sd 10.4)	0.55 (sd 0.02)	0.46 (sd 0.01)	9.85 (sd 1.96)	25.15 (sd 2.22)
Control 2	43.0 (sd 1.4)	0.55 (sd 0.01)	0.50 (sd 0.02)	15.02 (sd 0.95)	25.83 (sd 1.95)
Control 3	53.0 (sd 1.7)	0.45 (sd 0.02)	0.43 (sd 0.01)	16.32 (sd 0.67)	38.95 (sd 11.96)
Control 4	48.4 (sd 8.7)	0.50 (sd 0.03)	0.44 (sd 0.05)	14.40 (sd 0.32)	16.63 (sd 2.88)

Trends in the morphology of the collagen network are not unique. Since we analyze thin histological slides, the handling of these slides could potentially alter the tissue microstructure. Furthermore, the slides are taken transversely to the skin surface and some of the network morphologies are not captured within this plane. A more reliable measurement would be a volumetric imaging approach such as second-harmonic generation (Yasui et al., 2009), which we intend to do in the near future. Nonetheless, even with the limitations of our current approach, some trends emerge: Our analysis suggests that the papillary dermis, the top sublayer of the dermis, is not affected by the expansion protocol. In the reticular dermis, the bottom sublayer, coherency decreases in the expanded skin. A more careful investigation is needed to fully characterize the change in collagen microstructure over time as a result of applied stretch. Another area of future investigation is measuring the change in mechanical properties during skin growth with

noninvasive tools (Weickenmeier et al., 2015).

This study is not without its limitations, some of which have already been acknowledged. The three-dimensional photography system was compared to geometries generated with multi-view stereo, and we verified that both methods produced the same results. We have shown that the multi-view stereo reconstruction has errors that are on average 2% but can reach 10% in a small number of cases (Buganza Tepole et al., 2015a). We thus expect a similar measurement error in the results presented here. Another limitation is the small number of animals used in the experiments. Nonetheless, the results shown here align with our previous reports. Furthermore, even though the number of animals is small, each grid offers 121 data points. The challenge we face is that each of these points undergoes a different growth trajectory, and a direct comparison of the different deformation components is not possible. To address this, we need to parameterize the growth rate as a

function of deformation and solve an inverse problem to identify the best parameters that describe the data. Such approach would then allow a proper statistical analysis based on the growth trajectories of all 121 points per patch. This inverse problem is one of our next goals. Finally, the methodology still lacks a more comprehensive analysis of the cell scale. This work shows an important step in that direction. Before, we only measured tissue scale information. Here, we have introduced the histological analysis to better understand the remodeling of skin during tissue expansion. Still, more work in this direction is needed in order to identify the cellular mechanisms governing the observed histological changes.

5. Conclusions

This study establishes a methodology to study skin deformations and growth in a porcine model. Traditionally, *in vitro* systems have been used to characterize skin mechanotransduction. However, such experiments are unable to capture the complex biological response *in vivo*. Three-dimensional photography and isogeometric kinematic analysis enables tracking deformations of sizable skin patches, non-invasively, *in vivo*, and over long periods of time. Using the multiplicative split of the deformation gradient into elastic and growth contributions and accounting for prestrain and natural growth allows us to precisely quantify the differences of tissue expansion protocols for varying inflation timing and inflation volume. We found that larger volumes induce a heterogeneous deformation pattern characterized by large deformation at the apex and progressively less deformation toward the periphery of the expanded area. The expander-induced growth field for the large inflation volumes aligned with the total deformation patterns. For the small inflation volumes, the total deformation and expander-induced growth fields were more homogeneous. Overall, the apical points in the large volume models showed the greatest amount of expansion-induced growth. Further work is needed to elucidate the biological mechanisms that link the observed macroscopic effects to the underlying cellular mechanisms. Our histological analysis is a first step in this direction. It confirms previous observations that the epidermis becomes thicker upon tissue expansion. The exact mechanisms of skin growth and remodeling remain a topic of further investigation.

Acknowledgements

This work was supported by NIH grant 1R21EB021590-01A1 to Arun Gosain and Ellen Kuhl.

References

Alex, J.C., Bhattacharyya, T.K., Smyrniotis, G., O'Grady, K., Konior, R.J., Toriumi, D.M., 2001. A histologic analysis of three-dimensional versus two-dimensional tissue expansion in the porcine model. *Laryngoscope* 111 (1), 36–43.

Austad, E.D., Pasyk, K.A., McClatchey, K.D., Cherry, G.W., 1982. Histomorphologic evaluation of guinea pig skin and soft tissue after controlled tissue expansion. *Plast. Reconstr. Surg.* 70 (6), 704–710.

Bakhsheekia, A., 2013. Ten-year experience in face and neck unit reconstruction using tissue expanders. *Burns* 39 (3), 522–527.

Beauchene, J.G., Chambers, M.M., Peterson, A.E., Scott, P.G., 1989. Biochemical, biomechanical, and physical changes in the skin in an experimental animal model of therapeutic tissue expansion. *J. Surg. Res.* 47 (6), 507–514.

Buganza Tepole, A., Ploch, C.J., Wong, J., Gosain, A.K., Kuhl, E., 2011. Growing skin - A computational model for skin expansion in reconstructive surgery. *J. Mech. Phys. Solids* 59, 2177–2190.

Buganza Tepole, A., Gart, M., Purnell, C.A., Gosain, A.K., Kuhl, E., 2015a. Multi-view stereo analysis reveals anisotropy of prestrain, deformation, and growth in living skin. *Biomech. Mod. Mechanobiol.* 14 (5), 1007–1019.

Buganza Tepole, A., Kabaria, H., Bletzinger, K.U., Kuhl, E., 2015b. Isogeometric Kirchhoff-Love shell formulations for biological membranes. *Comput. Methods Appl. Mech. Eng.* 293, 328–347.

Buganza Tepole, A., Gart, M., Purnell, C.A., Gosain, A.K., Kuhl, E., 2016. The incompatibility of living systems: characterizing growth-induced incompatibilities in expanded skin. *Ann. Biomed. Eng.* 44 (5), 1734–1752.

Buganza Tepole, A., Vaca, E.E., Purnell, C.A., Gart, M., McGrath, J., Kuhl, E., Gosain, A.K., 2017. Quantification of Strain in a Porcine Model of Skin Expansion Using Multi-View

Stereo and Isogeometric Kinematics. *JoVE (J. Vis. Exp.)* 122, e55052.

Camison, L., Bykowski, M., Lee, W.W., Carlson, J.C., Roosenboom, J., Goldstein, J.A., Losee, J.E., Weinberg, S.M., 2017. Validation of the Vectra H1 portable three-dimensional photogrammetry system for facial imaging. *Int. J. Oral. Maxillofac. Surg.* <http://dx.doi.org/10.1016/j.ijom.2017.08.008>.

Chen, L., Nguyen-Thanh, N., Nguyen-Xuan, H., Rabczuk, T., Bordas, S.P., Limbert, G., 2014. Explicit finite deformation analysis of isogeometric membranes. *Comput. Methods Appl. Mech. Eng.* 277, 104–130.

De Filippo, R.E., Atala, A., 2002. Stretch and growth: the molecular and physiologic influences of tissue expansion. *Plast. Reconstr. Surg.* 109, 2450–2462.

Derderian, C.A., Bastidas, N., Lerman, O.Z., Bhatt, K.A., Lin, S.E., Voss, J., Holmes, J.W., Levine, J.P., Gurtner, G.C., 2005. Mechanical strain alters gene expression in an *in vitro* model of hypertrophic scarring. *Ann. Plast. Surg.* 55 (1), 69–75.

Fuchs, E., Raghavan, S., 2002. Getting under the skin of epidermal morphogenesis. *Nat. Rev. Genet.* 3 (3), 199–209.

Gosain, A.K., Zochowski, C.G., Cortes, W., 2009. Refinements of tissue expansion for pediatric forehead reconstruction: a 13-year experience. *Plast. Reconstr. Surg.* 124 (5), 1559–1570.

Hughes, T.J.R., Cottrell, J.A., Bazilevs, Y., 2005. Isogeometric analysis: CAD, finite elements, NURBS, exact geometry and mesh refinement. *Comp. Methods Appl. Mech. Eng.* 194, 4135–4195.

Iwahira, Y., Maruyama, Y., 1993. Combined tissue expansion: clinical attempt to decrease pain and shorten placement time. *Plast. Reconstr. Surg.* 91 (3), 408–415.

Jiang, C., Shao, L., Wang, Q., Dong, Y., 2012. Repetitive mechanical stretching modulates transforming growth factor-beta induced collagen synthesis and apoptosis in human patellar tendon fibroblasts. *Biochem. Cell Biol.* 90 (5), 667–674.

Johnson, P.E., Kernahan, D.A., Bauer, B.S., 1988. Dermal and epidermal response to soft-tissue expansion in the pig. *Plast. Reconstr. Surg.* 81 (3), 390–395.

Khalatbari, B., Bakhsheekia, A., 2013. Ten-year experience in face and neck unit reconstruction using tissue expanders. *Burns* 39 (3), 522–527.

Kuhl, E., 2014. Growing matter: a review of growth in living systems. *J. Mech. Behav. Biomed. Mater.* 29, 529–543.

Leyva-Mendivil, M.F., Page, A., Bressloff, N.W., Limbert, G., 2015. A mechanistic insight into the mechanical role of the stratum corneum during stretching and compression of the skin. *J. Mech. Behav. Biomed. Mater.* 49, 197–219.

Leyva-Mendivil, M.F., Lengiewicz, J., Page, A., Bressloff, N.W., Limbert, G., 2017. Skin microstructure is a key contributor to its friction behaviour. *Tribol. Lett.* 65 (1), 12.

Limbert, G., 2014. State-of-the-art constitutive models of skin biomechanics. *Comput. Biophys. Skin* 25, 95–131.

Limbert, G., 2017. Mathematical and computational modelling of skin biophysics: a review. *Proc. R. Soc. A-Math. Phys. Eng. Sci.* 473, 1–39.

Marcus, J., Horan, D., 1990. Robinson J Tissue expansion: past, present and future. *J. Am. Acad. Dermatol.* 23, 813–825.

Mustoe, T.A., Bartell, T.H., Garner, W.L., 1989. Physical, biomechanical, histologic, and biochemical effects of rapid versus conventional tissue expansion. *Plast. Reconstr. Surg.* 83 (4), 687–691.

Neumann, Charles G., 1957. The expansion of an area of skin by progressive distention of a subcutaneous balloon: use of the method for securing skin for subtotal reconstruction of the ear. *Plast. Reconstr. Surg.* 19 (2), 124–130.

Pamplona, D.C., Velloso, R.Q., Radwanski, H.N., 2014. On skin expansion. *J. Mech. Behav. Biomed. Mater.* 29, 655–662.

Radovan, C., 1982. Breast reconstruction after mastectomy using the temporary expander. *Plast. Reconstr. Surg.* 69 (2), 195–206.

Rausch, M.K., Kuhl, E., 2013. On the effect of prestrain and residual stress in thin biological membranes. *J. Mech. Phys. Solids* 61 (9), 1955–1969.

Rezakhaniha, R., Agianniotis, A., Schrauwen, J.T., Griffa, A., Sage, D., Bouten, C.V., Van de Vosse, F.N., Unser, M., Stergiopoulos, N., 2012. Experimental investigation of collagen waviness and orientation in the arterial adventitia using confocal laser scanning microscopy. *Biomech. Model Mechanobiol.* 11 (3–4), 461–473.

Rivera, R., LoGiudice, J., Gosain, A.K., 2005. Tissue expansion in pediatric patients. *Clin. Plast. Surg.* 32, 35–44.

Rodriguez, E.K., Hoger, A., McCulloch, A.D., 1994. Stress-dependent finite growth in soft elastic tissues. *J. Biomech.* 27, 455–467.

Schindelin, J., Arganda-Carreras, I., Frise, E., Kaynig, V., Longair, M., Pietzsch, T., Preibisch, S., Rueden, C., Saalfeld, S., Schmid, B., Tinevez, J.Y., 2012. Fiji: an open-source platform for biological-image analysis. *Nat. Methods* 9 (July (7)), 676.

Silver, F.H., Siperko, L.M., Seehra, G.P., 2003. Mechanobiology of force transduction in dermal tissue. *Skin Res. Tech.* 9, 3–23.

Taber, L.A., 1995. Biomechanics of growth, remodeling, and morphogenesis. *Appl. Mech. Rev.* 48, 487–545.

Taber, L.A., Chabert, S., 2002. Theoretical and experimental study of growth and remodeling in the developing heart. *Biomech. Model Mechanobiol.* 1 (1), 29–43.

Timmenga, E.J., Schoorl, R., Klopper, P.J., 1990. Biomechanical and histomorphological changes in expanded rabbit skin. *Br. J. Plast. Surg.* 43 (1), 101–106.

Turin, S.Y., Ledwon, J., Bae, H., Buganza, Tepole, Topczewska, J., Gosain, A.K., 2018. Digital analysis yields more reliable and accurate measures of dermal and epidermal thickness in histologically processed specimens compared to traditional methods. *Exp. Dermatol. (in revision)*.

VanderKolk, C.A., McCann, J.J., Mitchell, G.M., O'Brien, B.M., 1988. Changes in area and thickness of expanded and unexpanded axial pattern skin flaps in pigs. *Br. J. Plast. Surg.* 41 (3), 284–293.

Wang, J.H.C., Thampatty, B.P., 2006. An introductory review of cell mechanobiology. *Biomech. Model Mechanobiol.* 5 (1), 1–16.

Wang, J.H.C., Thampatty, B.P., Lin, J.S., Im, H.J., 2007. Mechanoregulation of gene expression in fibroblasts. *Gene* 391, 1–15.

Wong, V.W., Akaishi, S., Longaker, M.T., Gurtner, G.C., 2011. Pushing back: wound

- mechanotransduction in repair and regeneration. *J. Investig. Dermatol.* 131 (11), 2186–2196.
- Weickenmeier, J., Jabareen, M., Mazza, E., 2015. Suction based mechanical characterization of superficial facial soft tissues. *J. Biomech.* 48 (16), 4279–4286.
- Yang, M., Li, Q., Sheng, L., Li, H., Weng, R., Zan, T., 2011. Bone marrow-derived mesenchymal stem cells transplantation accelerates tissue expansion by promoting skin regeneration during expansion. *Ann. Surg.* 253 (1), 202–209.
- Yasui, T., Takahashi, Y., Ito, M., Fukushima, S., Araki, T., 2009. Ex vivo and in vivo second-harmonic-generation imaging of dermal collagen fiber in skin: comparison of imaging characteristics between mode-locked Cr: forsterite and Ti: sapphire lasers. *Appl. Opt.* 48 (10), D88–95.
- Zeng, Y.J., Xu, C.Q., Yang, J., Sun, G.C., Xu, X.H., 2003. Biomechanical comparison between conventional and rapid expansion of skin. *Br. J. Plast. Surg.* 56 (7), 660–666.
- Zollner, A.M., Holland, M.A., Honda, K.S., Gosain, A.K., Kuhl, E., 2013. Growth on demand: reviewing the mechanobiology of stretched skin. *J. Mech. Behav. Biomed. Mat.* 28, 495–509.